

Geophysical Research Letters

RESEARCH LETTER

10.1029/2018GL081867

Key Points:

- Atmospheric thermal stratifications show similar structures over varying surface elevations under RCE
- This similarity is largely due to the invariance of entrainment/detrainment rates
- This similarity is supported by reanalysis data and provides a useful simplification for climate research

Supporting Information:

- Supporting Information S1

Correspondence to:

D. Ma,
dingma3277@gmail.com

Citation:

Nie, J., Xia, Y., Hu, S., Yuan, W., Yang, J., & Ma, D. (2019). Similarity among atmospheric thermal stratifications over elevated surfaces under radiative-convective equilibrium. *Geophysical Research Letters*, 46. <https://doi.org/10.1029/2018GL081867>

Received 4 JAN 2019

Accepted 24 FEB 2019

Accepted article online 1 MAR 2019

Similarity Among Atmospheric Thermal Stratifications Over Elevated Surfaces Under Radiative-Convective Equilibrium

Ji Nie¹ , Yan Xia¹, Shineng Hu² , Wei Yuan³, Jun Yang¹ , and Ding Ma⁴ 

¹Department of Atmospheric and Oceanic Sciences, Peking University, Beijing, China, ²Scripps Institution of Oceanography, University of California, San Diego, La Jolla, CA, USA, ³Aviation Meteorological Center, CAAC, Beijing, China, ⁴Earth Institute, Columbia University, New York, NY, USA

Abstract An air column under radiative-convective equilibrium is studied here to understand equilibrium climate over different surface elevations. Cloud-resolving model (CRM) simulations show that atmospheric thermal stratifications exhibit similar structures when expressed in σ coordinates over varying surface elevations under radiative-convective equilibrium. A zero-buoyancy plume model that reproduces CRM results is used to interpret related processes. As surface pressure decreases, decreased pressure on a certain σ level leads to decreases of moist adiabatic temperature lapse rate, which largely cancel the increases of moist adiabatic lapse rate by temperature decreases. Meanwhile, the invariance of convective entrainment/detrainment rates keeps the deviation of environmental temperature lapse rate from moist adiabatic approximately invariant, result in similar thermal stratifications under varying surface pressures. A comparison of thermodynamic profiles over the Tibetan Plateau with those over plains in reanalysis confirms the similarity found in CRM simulations. This similarity provides a useful simplification for representing the effects of convection.

Plain Language Summary What constrains the vertical structure of the atmosphere over different surface elevations? Here it is found that the atmospheric vertical stratification exhibits similar structures in a specific vertical coordinate normalized by the mass of the column. Cloud-resolving numerical models are used to understand this similarity, which has significant implications for modeling convection in global climate models.

1. Introduction

The Earth's land surface elevation varies widely from about 400 m below sea level at the Dead Sea to over 8 km in the Himalayas. As the surface elevation varies, the air mass above it changes, as do the radiative transfer (e.g., the scattering of shortwave radiation and the absorption and emission of longwave radiation) and convective processes (e.g., the condensation of water vapor) in the atmosphere, leading to changes in the atmospheric thermal structure. Elevated surfaces are commonly associated with local temperature peaks over surrounding regions in the free troposphere. This phenomenon, usually referred to as “elevated heating,” has been claimed to drive regional to large-scale circulations, such as the Tibet Plateau on the Asian monsoon (e.g., Wu, 2007; Wu & Zhang, 1998), or the Bolivian Plateau on the South American monsoon (Rao & Erdogan, 1989). Although recent studies challenged the dominant role of elevated heating on forcing regional monsoons (e.g., Boos & Kuang, 2010; Ma et al., 2014; Molnar et al., 2010), the fundamental question of what sets the thermal structures over high elevations still remains. Understanding the effects of surface pressure on climate also has important implications on paleoclimate and planetary sciences; the total masses of the atmospheres of Earth and some other planets are known to have varied through their evolution history. For example, the atmospheric surface pressure of Earth may have been only about 0.5 bar during the Archaean Eon (Marty et al., 2014; Som et al., 2016), while it could have reached 1.2 bar during the Phanerozoic Eon (Poulsen et al., 2015). On Mars, the current atmospheric pressure is only 0.006 bar, but it could be as high as 1–2 bar during early Mars (Kite et al., 2014).

A starting point for examining the dependence of atmospheric states on either the surface elevation or surface pressure is the consideration of an air column under radiative-convective equilibrium (RCE), in which

radiative cooling is balanced by convective heating without any complications due to large-scale circulations. An early study conducted by Molnar and Emanuel (1999) provided two theoretical limits under RCE. Under the limit in which the atmosphere is transparent to radiation, the surface temperature (T_s) would be the black-body temperature, and it would be independent of the surface elevation. Under the other limit, in which the atmosphere is very opaque to longwave radiation, the tropopause temperature would be nearly fixed (Held, 1982); since convection would maintain the tropospheric temperature close to a moist adiabatic profile, T_s would decrease with the surface elevation following the moist adiabatic lapse rate. The authors argued that the real-world situation should exist between these two limits, and their assertion was supported by simulations using a single-column model, showing that T_s decreases with the surface elevation at a rate of 2 K/km. Recently, Hu and Boos (2017a), hereafter HB17, examined this problem using a cloud-resolving model (CRM), which represents convective processes more realistically than does a single-column model. HB17 adopted the climate feedback diagnostic framework to quantify the radiative forcings due to different physical processes and concluded that changes in the previously overlooked tropospheric lapse rate together with variations in shortwave and longwave radiative forcings due to reductions in air masses account for the observed decreases in T_s with increases in the surface elevation.

This paper seeks to understand the dependence of atmospheric thermodynamic states on the surface elevation or surface pressure (P_s). We first note that atmospheric thermodynamic profiles in CRM simulations with different surface elevations under RCE share similar vertical structures when expressed in coordinates of pressure normalized by surface pressure (the σ coordinate). Then, we show that a zero-buoyancy plume model is able to reproduce the similarity in the thermal stratification exhibited in CRM simulations largely because the entrainment and detrainment rates are nearly invariant in the σ coordinate. Subsequently, reanalysis data are compared with the CRM simulations, lending support to our main conclusions. Utilizing the above-mentioned similarity, we demonstrate that the dependence of T_s on P_s can be estimated reasonably well with only radiative transfer calculations. This study provides an intuitive interpretation for the dependence of atmospheric states on the surface height under RCE in addition to a simple but useful approximation for climate studies.

2. Numerical Experiments and Data

The numerical simulations analyzed in this paper are adopted from the ones performed in HB17. A group of CRM simulations under RCE is examined. The CRM used herein is the System for Atmospheric Modeling, which solves the anelastic equations of motion with prognostic liquid water moist static energy, total non-precipitating water, and total precipitating water (Khairoutdinov & Randall, 2003). The Earth's rotation is not included in the simulations. In the simulations, all other parameters or settings are fixed, but P_s decreases from 1,008 to 500 hPa. In all experiments, the CO_2 concentrations are fixed at 355 ppmv throughout the air column, and the O_3 profiles are kept the same with respect to the surface; thus, the total column masses of CO_2 and O_3 will change as P_s changes. The insolation is specified to be 364 W/m^2 , the annual mean value is fixed at 30°N, and the surface albedo is specified to be 0.24. The control case with $P_s = 1,008$ hPa represents an air column over the sea surface level, whereas the perturbed cases have P_s values of 890, 790, 710, 600, and 500 hPa, which are approximately equivalent to surface heights of 1, 2, 3, 4, and 6 km, respectively.

Monthly mean European Centre for Medium-Range Weather Forecasts Re-Analysis (ERA)-Interim reanalysis data (Dee, 2011) and monthly mean Global Precipitation Climatology Project (GPCP) precipitation data (Huffman, 2001) are analyzed to support the results from the numerical simulations. The GPCP precipitation data range from 1979 to 2013 and have a horizontal resolution of $2.5^\circ \times 2.5^\circ$. The European Centre for Medium-Range Weather Forecasts Re-Analysis data range from 1979 to 2017, and they are converted from their original resolution of $0.7^\circ \times 0.7^\circ$ to a resolution of $2.5^\circ \times 2.5^\circ$.

3. Results

3.1. Similarity Among Atmospheric Thermal Stratifications

As P_s decreases from 1,000 to 500 hPa, T_s decreases from 304.5 to 291.5 K with $\frac{dT_s}{dP_s} \approx 2.46$ K per 100 hPa (Figure 1), consistent with previous study (Molnar & Emanuel, 1999). These results indicate that cooling due to decreases in the concentrations of greenhouse gasses (water vapor and CO_2) dominates over warming due to the weakened scattering of shortwave radiation. In addition, a decrease in the pressure narrows the absorption lines of greenhouse gasses, even if the partial pressures of greenhouse gasses remain fixed

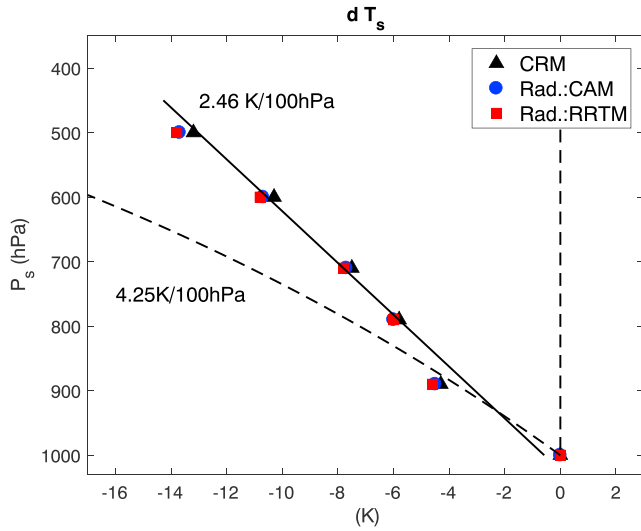


Figure 1. dT_s as a function of P_s . The two dashed lines are the two theoretical limits, in which T_s is either independent of P_s or decreases with P_s following the moist adiabatic lapse rate. The markers are the values of dT_s from cloud-resolving model (CRM) simulations estimated using the community atmosphere model (CAM) and rapid radiative transfer model (RRTM) radiative transfer codes, respectively. The black solid line is the best linear fitting of the CRM results.

formation as follows. The temperature anomalies of the perturbed cases relative to the control case ($dT(\sigma)$) are nearly independent of σ . This allows us to use a constant dT (the average of $dT(\sigma)$) to describe the shift in the T profile for each perturbed case. By adding dT to the corresponding perturbed T profiles, all the T profiles nearly collapse into the T profile of the control case (Figure 2d). Similarly, by multiplying the q profiles by their corresponding constant factors (β), they also nearly collapse into one line. If we mark the control case with the subscript 0 and a perturbed case with the subscript 1, one may make the following three approximations (denoted (A1)–(A3)) based on Figures 2d–2f:

$$T_0(\sigma) \approx T_1(\sigma) + dT, \quad (\text{A1})$$

$$q_0(\sigma) \approx \beta q_1(\sigma), \quad (\text{A2})$$

$$R_{H,0}(\sigma) \approx R_{H,1}(\sigma). \quad (\text{A3})$$

The above similarity in the σ coordinates implies that atmospheric thermal stratifications are strongly constrained by processes that depend weakly on P_s . The current transformation in equations (A1)–(A3) is similar to the vertical shift transformation (VST) in Singh and O’Gorman (2012). Let the rescaling parameter (β in VST) be the surface pressure factor (α here); the VST also shifts the T and q profiles upward correspondingly. However, in VST the transformation of q is a pure shift (keeping its shape), and the transformation of T has an adjustment that is a function of pressure in order to be consistent with geopotential’s rescaling (equations (9), (13d), and (13e) in Singh & O’Gorman, 2012). On the contrary, here the transformation of T keeps its shape with a vertically constant adjustment (A1), while the transformation of q has an adjustment of multiplication, which modifies its shape (A2).

Approximation (A2) can be deduced with (A1) and (A3) because q and R_H are not independent of each other. The specific humidity of a perturbed case can be expressed as $q_1(\sigma) = R_{H,1}(\sigma) q_v^*(T_1, p_1) \approx R_{H,1}(\sigma) \frac{R_d}{R_v} \frac{e^*(T_1)}{\sigma P_{s,1}}$, where $e^*(T)$ is the saturation water vapor pressure and R_v is the gas constant of water vapor. Let α denote the ratio of a perturbed case $P_{s,1}$ to the control case $P_{s,0}$ ($\alpha = \frac{P_{s,0}}{P_{s,1}}$), where the ratio between q_0 and q_1 at a particular σ level is

$$\beta = \frac{q_0(\sigma)}{q_1(\sigma)} = \frac{R_{H,0}}{R_{H,1}} \frac{P_{s,1}}{P_{s,0}} \frac{e^*(T_0)}{e^*(T_1)} \approx \frac{1}{\alpha} e^{cdT}. \quad (1)$$

(i.e., the pressure broadening effect; Pierrehumbert, 2010), thereby inducing an additional negative radiative forcing (HB17). For most cases, the differences in the surface temperature from the control case (dT_s) are located within the two theoretical limits suggested by Molnar and Emanuel (1999), dashed lines in Figure 1; however, neither theoretical limit provides an accurate approximation for $\frac{dT_s}{dP_s}$.

Upon examining the temperature (T), specific humidity (q), and relative humidity (R_H) profiles in the conventional pressure (p) coordinates following previous studies (Hu & Boos, 2017a; Molnar & Emanuel, 1999), prominent dependencies of these profiles on P_s are revealed (Figures 2a–2c). At the same pressure level, the value of T over an elevated surface (small P_s) is much higher than that over sea level. Correspondingly, the temperature lapse rate per unit pressure or height (and thus the dry static stability) increases significantly as P_s decreases, introducing complexities into many dynamic problems, such as those involving atmospheric waves and climate feedbacks (HB17).

When considering problems with varying P_s , the σ coordinate ($\sigma = p/P_s$) is a more convenient coordinate choice because it takes changes in the total air mass into account. The σ coordinate is related to the z coordinate by $\sigma = e^{-\int_0^z \frac{g}{R_d T} dz}$, where R_d is the gas constant of dry air and z is the height relative to the elevated surface rather than the sea surface level. The thermodynamic profiles exhibit remarkable similarities when plotted in the σ coordinate (Figures 2d–2f). The temperature and relative humidity profiles can be made to look the same with a simple transfor-

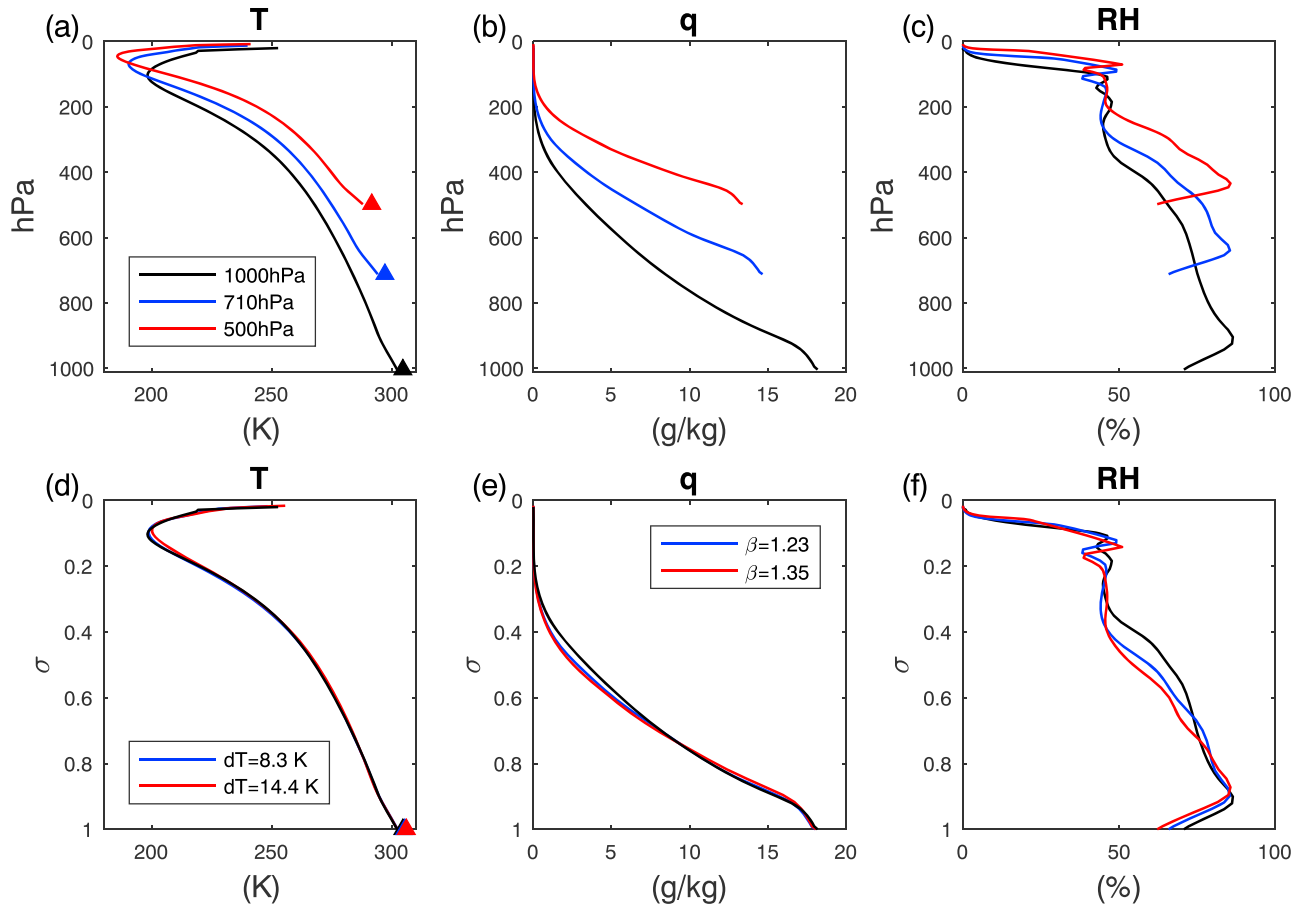


Figure 2. The T , q , and R_H profiles for cases with varying P_s in the pressure coordinate (a–c) and in the σ coordinate (d–f). In (d), the T profiles of perturbed cases are shifted horizontally by a constant dT . In (e), the q profiles of perturbed cases are multiplied by a constant factor β . dT and β are calculated by minimizing the residual errors.

In the above derivation, we use the Clausius-Clapeyron (CC) relation to approximate the saturation water vapor pressure; thus, $e^*(T) \approx e^*(T_c)e^{c(T-T_c)}$, where $c = \frac{L_w}{R_v T_c^2}$, T_c is a reference temperature (e.g., 300 K) and L_w is the latent heat of condensation. Over the range of temperatures examined herein, the CC scaling has $c \approx 6.5\text{--}7\%/K$ (we take $c \approx 6.8\%/K$ hereafter). Equation (1) provides a reasonable estimation of β given dT . For example, for the case where $P_{s,1} = 500$ hPa, equation (1) gives $\beta = 1.33$, which is very close to the value estimated by minimizing the residual error (Figure 2e). Thus, in the following, we will focus on explaining the similarities between the T and R_H profiles.

3.2. Understanding the Similarity With a Zero-Buoyancy Plume Model

We use a conceptual model, the zero-buoyancy plume model (Romps, 2014; Singh & O’Gorman, 2013; Singh et al., 2017), to examine the dependence of thermal stratification on P_s . This model describes the properties of a bulk plume, which represents the ensemble of convective cloud updrafts (Siebesma & Cuijpers, 1995). The thermodynamic variable of the moist static energy ($h = c_p T + gz + L_v q$, where c_p is heat capacity at constant pressure and g denotes gravitational acceleration) is used to help the derivation, as h is nearly conserved in moist adiabatic processes. The vertical changes in h within a convective plume are due only to the entrainment of environmental air:

$$\frac{dh_c}{dz} = -\epsilon(h_c - h), \quad (2)$$

where ϵ is the effective fractional entrainment rate and the subscript c refers to the convective plume, while subscripts for environmental variables are omitted. Because the difference between the temperature of a convective updraft and temperature of the surrounding environment is very small (<0.5 K for all cases in our simulation), we apply the zero-buoyancy approximation of $T \approx T_c$ (Bretherton & Park, 2008) on equation (2),

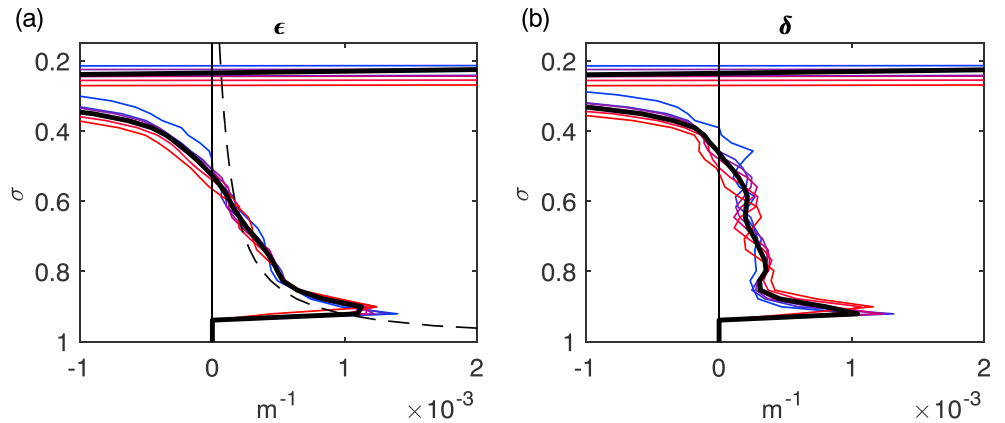


Figure 3. The thick colored lines are ϵ (a) and δ (b) diagnosed from the cloud-resolving model results using h . A change in the line color from blue to red corresponds to the case in which P_s changes from 1,000 to 500 hPa. The black solid lines are the means of all cases. The black dashed line in (a) is the idealized ϵ profile used in the plume model.

leading to an expression for the temperature lapse rate:

$$\frac{dT}{dz} = -\frac{g}{C_p} - \frac{L_v}{C_p} \frac{dq_v^*(T)}{dz} - \epsilon \frac{L_v}{C_p} q_v^*(T)(1 - R_H). \quad (3)$$

The first two terms on the right-hand side are the dry adiabatic lapse rate and the reduction of lapse rate due to latent heat release, and their sum is the moist adiabatic lapse rate. The third term is the modification due to entrainment of subsaturated air (Singh & O’Gorman, 2013). Given ϵ and R_H , equation (3) is an ordinary differential equation for T that can be integrated upward with initial conditions at the surface level. The zero-buoyancy plume model (equation (3)) serves as a tool for us to understand the dependence of the T structure on P_s .

We first calculate the T profiles with equation (3) and compare them with those from CRM simulations to validate the model. The R_H profile is specified as the mean of all cases from the CRM simulations, and the surface layer conditions are taken from the CRM results. ϵ may be diagnosed using conserved variables from the CRM simulations (Nie et al., 2016; Romps, 2010; Siebesma & Cuijpers, 1995). However, the diagnosed ϵ (Figure 3a) is negative in the middle to upper troposphere, where the environmental h starts to increase with the height and the preferential detrainment of convective updrafts becomes important. This unphysical negative ϵ , which has been reported by previous studies (Kuang & Bretherton, 2006; Romps, 2010), is a shortcoming of the bulk plume assumption. Instead, an idealized profile of $\epsilon = \hat{\epsilon}/z$ is used herein following (Holloway & Neelin, 2009; Singh & O’Gorman, 2013). We set $\hat{\epsilon} = 0.7$ to have a reasonable match with the results of the CRM control case. ϵ is assumed to be zero below the cloud base, defined as the condensation level for surface layer air. The dashed line in Figure 3a indicates that the idealized ϵ (plotted in the σ coordinate based on the conversion of $z(\sigma)$ for the control case) matches the diagnosed ϵ from the lower to the middle troposphere and approaches zero in the upper troposphere. Note that the diagnosed ϵ s of all the perturbed cases are very close to that of the control case, thereby indicating invariance of ϵ in the σ coordinate with changes in P_s . Based on these diagnoses, in the calculations of the perturbed cases with the plume model, we use the same $\epsilon(\sigma)$ profile in Figure 3a (using $\epsilon = \hat{\epsilon}/z$ gives very similar results; however, using fixed $\epsilon(\sigma)$ profile is conceptually more consistent with the idea of using the σ coordinate as the vertical coordinate.)

The zero-buoyancy plume model with the above parameters reproduces the T profiles from the CRM simulations reasonably well. For the control case (Figure 4a), the temperature profiles from the CRM simulations and those from the plume model are very close to each other. The error in the plume model becomes appreciable near the tropopause layer, where radiative processes take control of the temperature stratification. Figure 4b shows that the CRM-simulated temperature lapse rates in the σ coordinate ($\Gamma_\sigma = \frac{dT}{d\sigma}$) of the perturbed cases are very close to that of the control case, consistent with the T similarity shown in Figure 2d. Figure 4c plots the differences in Γ_σ between the plume model and CRM simulation results. The plume model also reproduces the CRM results well for the perturbed cases. Over most of the troposphere, the errors

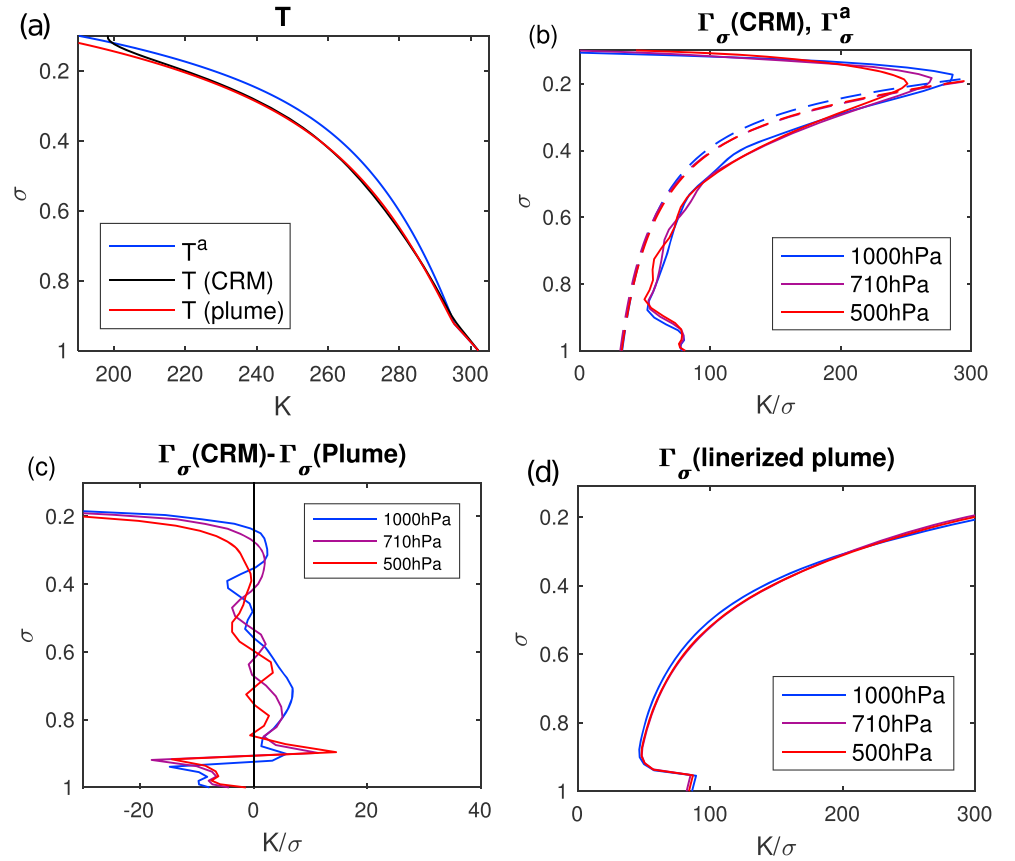


Figure 4. (a) The T profile for the control case from the cloud-resolving model (CRM) simulation and the plume model. The moist adiabatic temperature profile for an undiluted rising air parcel (T^a) is also plotted for comparison. (b) The values of Γ_σ from CRM simulations (solid lines) and the moist pseudoadiabatic lapse rate (Γ_σ^a) for air parcels initialized from the surface temperatures in these simulations (dashed lines). (c) The differences in Γ_σ between the plume model and the CRM simulations. (d) The values of Γ_σ from the linearized plume model.

are very small; however, the plume model again fails near the tropopause. The above results validate the ability of the zero-buoyancy model to capture the dependence of thermal profiles on P_s . To test the importance of the invariance of ϵ on the temperature similarity, a series of calculations with perturbed ϵ values are performed for the $P_s = 500$ hPa case. The results show that changes in ϵ can effectively change the temperature profiles (Figure S1 in the supporting information).

It is usually assumed that convection maintains temperature profiles to remain nearly neutral for moist convection, so that the temperature is close to the moist adiabatic temperature (T^a , where the superscript a denotes moist adiabatic), and the lapse rate is close to the moist adiabatic lapse rate (Γ_σ^a ; Emanuel et al., 1994). When P_s changes, the values of Γ_σ^a (dashed lines in Figure 4b) are also very close to each other (plots of Γ_σ^a as a function of T and σ can be found in Figure S2). One might tempt to reason that the similarity among the T profiles is due to the similarity in Γ_σ^a . However, this is only part of the story. As shown in Figure 4a, the differences between T and T^a ($\Delta T = T^a - T$) are distinct. These differences in the temperature are essential for the formation of convective available potential energy. Moreover, ΔT may depend on the states of convection; for example, Singh and O’Gorman (2013) showed that ΔT increases as the surface temperature increases (with a fixed surface pressure). The zero-buoyancy plume model takes ΔT into account by including the effects of saturation deficits and thus goes beyond the moist adiabatic approximation.

Next, we provide a linearized version of the plume model to elucidate the similarity among thermal stratifications. Using the CC scaling to approximate the saturation humidity function, we have $q_s^*(\sigma, T) \approx \frac{R_d}{R_v} \frac{e^*(T_c)}{\sigma P_s} e^{c(T-T_c)}$. Substituting this into equation (3), we can express Γ_σ as

$$\Gamma_\sigma = \frac{R_d T}{C_p \sigma} \frac{1 + df}{1 + f}, \quad (4)$$

where $f(T, \sigma) = \frac{L_v c}{C_p} q_v^*$ and $d(T, \sigma) = \frac{C_p}{g c} \left(\frac{g}{R_d T} + \epsilon(1 - R_H) \right)$. q_v^* is very important in determining the lapse rate, and it is a sensitive function of both the temperature and the pressure; therefore, in the derivation of equation (4) from equation (3), we group the q_v^* terms in f and group the rest of the terms in d . $d \approx 0.3$ is approximately constant throughout the troposphere, and f decreases from 2 in the lower troposphere to 0 in the upper troposphere. The values of Γ_σ calculated with equation (4) capture the main features of Γ_σ from the CRM simulations (Figure 4d). To show the sensitivity of Γ_σ to changes in P_s , we compare Γ_σ from a perturbed case with that from the control case at the same σ level:

$$\frac{\Gamma_{\sigma,1}}{\Gamma_{\sigma,0}} = \frac{T_1}{T_0} \frac{1 + d f_1}{1 + d f_0} \frac{1 + f_0}{1 + f_1}. \quad (5)$$

With the same ϵ and R_H , the changes in d are very small; thus, we set $d_1 \approx d_0$ in equation (5). In the following, we will relate changes in f to temperature shifts dT and show that these changes are ineffective at changing Γ_σ .

Note that $\frac{T_0 - T_1}{T_0} = \frac{dT}{T_0} \ll 1$ and $\frac{f_0 - f_1}{f_0} = (\beta - 1) \ll 1$. By linearly expanding equation (5) and keeping only the first-order perturbation terms, we have

$$\frac{\Gamma_{\sigma,1}}{\Gamma_{\sigma,0}} \approx 1 + \left(\frac{f_0}{1 + f_0} - \frac{d f_0}{1 + d f_0} \right) (\beta - 1) - \frac{dT}{T_0}. \quad (6)$$

Also note that $P_{s,1} - P_{s,0} = -\left(\frac{dT_s}{dP_s}\right)^{-1} dT$; substituting this into equation (1) and linearizing the exponential term of e^{cdT} , we have $\beta - 1 \approx \left(c - \frac{1}{P_{s,0}} \frac{dT_s}{dP_s}\right) dT$. Taking typical values of $f_0 \sim 1$, $d \sim 0.3$, and $\frac{dT_s}{dP_s} = 2.5 \times 10^{-4} \text{ K/Pa}$, equation (6) results in

$$\frac{\Gamma_{\sigma,1}}{\Gamma_{\sigma,0}} \approx 1 + 0.005 dT. \quad (7)$$

For the range of dT within ± 10 K, the change in $\frac{\Gamma_{\sigma,1}}{\Gamma_{\sigma,0}}$ is within $\pm 5\%$. Two main reasons account for the insensitivity of the lapse rate to the surface pressure. One reason is the invariance of the entrainment rates and R_H (thus, d in equation (4) changes very little). The other reason is the canceling effects that decreases both in T and in P have on the moist adiabatic lapse rate (expressed as f or q_v^* in equation (4) or as $\beta - 1$ in the perturbation of equation (6)). With a fixed pressure, a decrease in the temperature leads to a decrease in q_v^* and an increase in the moist adiabatic lapse rate. However, at a fixed σ level, a decrease in p due to a decrease in P_s leads to an increase in q_v^* and a decrease in the moist adiabatic lapse rate. These two effects largely compensate each other, thereby reducing the sensitivity of the moist adiabatic lapse rate to P_s .

The above analyses examine the similarity among T profiles given ϵ and R_H . In the following, we will present a qualitative argument for the approximate invariance of R_H with respect to changes in P_s , although providing a corresponding theory for R_H is beyond the scope of this study. Using the zero-buoyancy plume model and considering the energy balance of the environmental air, Romps (2014) reached an expression for R_H , which is written in the σ coordinate as follows:

$$R_H(\sigma) = \frac{\delta}{\delta + \frac{g\sigma}{R_d T} \partial_\sigma \ln q_v^*}, \quad (8)$$

where δ is the effective fractional detrainment rate. Equation (8) states that the environmental R_H is determined by the saturation humidity in clouds (q_v^*) and the rate at which excessive moisture moves from clouds to the environment (δ). Under RCE, $\frac{g\sigma}{R_d T} \partial_\sigma \ln q_v^*$ is small relative to δ , corresponding to the fact that the free troposphere R_H is approximately 70–80%. Now, consider the form of R_H based on equation (8). The CRM diagnoses show that, similar to ϵ , δ is also nearly invariant when P_s changes (Figure 3b). The other factor in the denominator, q_v^* , as is reasoned in the paragraph above, varies little at the same σ level as P_s changes due to the canceling effects of decreases both in the temperature and in the pressure. Thus, R_H is also insensitive to changes in P_s expressed in the σ coordinate.

3.3. Support From Reanalysis Data

Although the idealized form of RCE does not exist in the real atmosphere, it may be an acceptable approximation for the atmosphere averaged over large domains (i.e., so that the effects of large-scale circulations

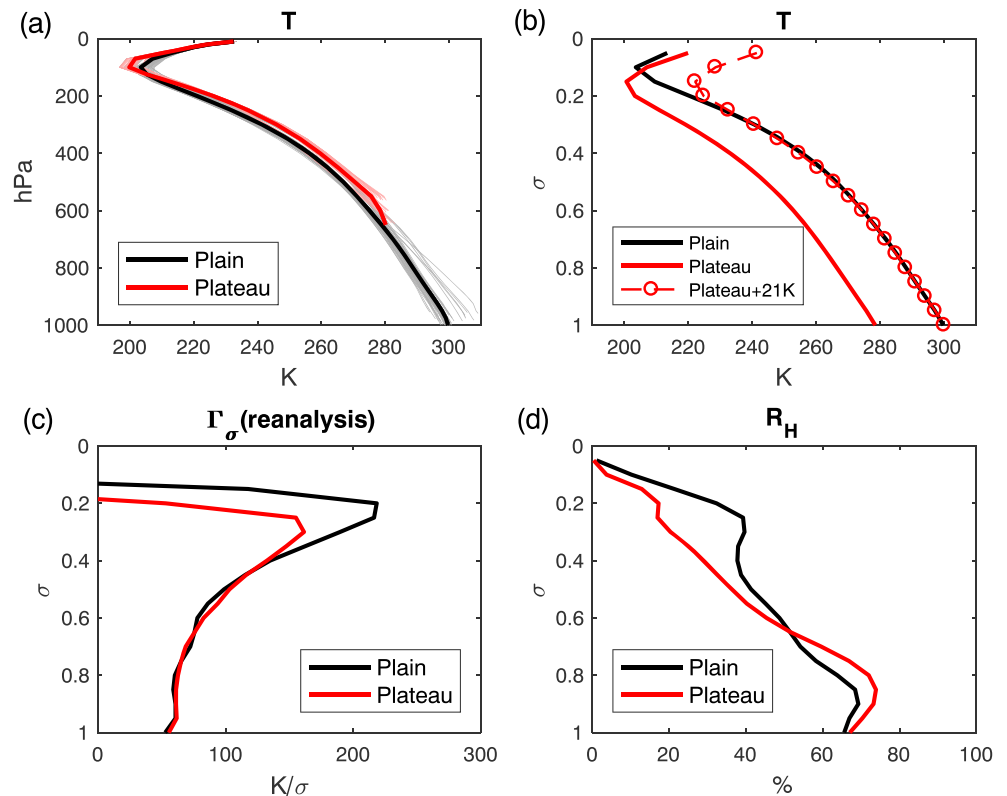


Figure 5. (a) The thin pink lines and thin gray lines are the T profiles over the Tibetan Plateau and over plains, respectively, in the p coordinate. The thick lines are the means of the thin lines. (b) The T profiles in the σ coordinate. (c) The values of Γ_σ over the Tibetan Plateau and over plains. (d) The R_H profiles over the Tibetan Plateau and over plains. All the results are from the ERA-Interim reanalysis data.

are canceled out and become less important) and over long periods (i.e., in an equilibrium state). For example, the average thermal states of the tropical belt may be viewed under RCE (e.g., Silvers et al., 2016). Based on the above guidelines, to test whether the similarity observed in the CRM simulations can be found in reanalysis data, we compare the summer (June through August) monthly mean T profiles over the Tibetan Plateau with those over plains. The air columns over the Tibetan Plateau defined as grids with $P_s < 650$ hPa cover an area of approximately 2.1×10^6 km² from 30°N to 40°N (mean latitude is 33.4°N). The air columns over plains are defined as land grids in the same latitude band with $P_s > 950$ hPa and with a monthly mean GPCP precipitation exceeding 2 mm/day. The latitude criterion is the same for the grids with similar insolation. The precipitation criterion is used to ensure that the air column is convectively active so that the convective quasi-equilibrium approximation holds (Arakawa & Schubert, 1984; Emanuel et al., 1994; Nie et al., 2010). The grids of the plains cover an area of approximately 3.5×10^6 km² (mean latitude is 33.7°N), located mostly over East China and the southeastern United States (a sensitivity test in which the plains grids include only those over East China reveals similar results, as shown in Figure S3). The summer season is chosen because convection is the most active over the Tibetan Plateau during this time and the northern subsidence branch of the Hadley cell is the weakest. The following results are not sensitive to the criteria of P_s or precipitation and hold only for the summer season.

Two clusters of T profiles over the Tibetan Plateau and plains are separated from each other (Figure 5a). The elevated heating effect is obvious, but it is not as large as that observed in the CRM results; this difference is arguably caused by the high surface albedo over the Tibetan Plateau (Hu & Boos, 2017b). In the σ coordinate, the T profiles show similar structures (Figures 5b and 5c) to the levels below the tropopause, which is similar to the structures seen in the CRM results. The similarities among the R_H profiles (Figure 5d) are not as good as those in the CRM results, especially in the upper troposphere. However, the moisture content in the upper troposphere is very low, and small errors may be expressed as large deviations in R_H . Overall, this

comparison between the thermal profiles over the Tibetan Plateau and plains in the reanalysis data lends support to the similarity found in the CRM simulations.

3.4. Using the Similarity to Estimate the RCE T_s

The similarity among atmospheric thermal stratifications absorbs the complexity of convective processes and may serve as a useful approximation for climate problems with changes in P_s . Here we demonstrate that one can estimate the dependence of T_s on P_s reasonably well using only radiative transfer calculations using this similarity.

Let the T and q profiles of the control case be known. Here we want to estimate the equilibrium climate of a perturbed case. By assuming constant temperature differences between the surface temperature and surface air temperature ($T_s \approx T(\sigma = 0) + 2K$; this approximation holds for all cases) and using approximations (A1)–(A3), the only unknown for the perturbed case is the shift in the temperature profile (dT). Since we are considering the equilibrium state, we therefore seek the value of dT leading to radiative energy balance at the top of the atmosphere. Two radiative transfer models are used to calculate the top of the atmosphere radiative fluxes using T_s , T , and q : One is adopted from the community atmosphere model (Kiehl et al., 1998), which is the same model used in the CRM simulations, and the other is the rapid radiative transfer model (Mlawer et al., 1997). The estimated dT values using both models are very close to those obtained in the CRM simulations (Figure 1).

A caveat of the above calculation is that cloud radiative effects are neglected. As P_s varies, the changes in the longwave or shortwave cloud radiative forcings are $\sim 15 \text{ W/m}^2$ with opposite signs. Due to the canceling effects of longwave and shortwave cloud radiative forcings, changes in the net cloud radiative forcing are relatively small (from 0.5 W/m^2 at $P_s = 1,000 \text{ hPa}$ to 5.5 W/m^2 at $P_s = 500 \text{ hPa}$). In other cases where cloud radiative effects play important roles in the radiative energy balance, these radiative effects may need to be taken into account.

4. Conclusions and Discussion

The surface pressure, which reflects the total air mass, is an important yet overlooked controlling factor on the states of the Earth's atmosphere. For the present-day Earth, the surface elevation impacts the regional climate and drives atmospheric circulations. Large variations in the surface pressure over geologic time on Earth and on other planets have had significant implications for their atmosphere. This study examines the atmospheric thermal stratifications with changes in P_s under RCE while holding other factors fixed. CRM simulations show remarkable similarity among these thermal stratifications when viewed in the σ coordinate with varying P_s . A zero-buoyancy plume model can reproduce the variable thermodynamic profiles of these CRM simulations. Analyses of this simple model indicate that the invariance of the entrainment and detrainment rates largely contributes to the similarity among the thermal stratifications. Furthermore, the effects of decreasing temperatures and pressures on the lapse rate largely compensate each other. A comparison of the thermodynamic profiles over the Tibetan Plateau with those over plains in the reanalysis data lends support to the similarity found in the CRM simulations. This similarity, which implies that atmospheric thermal stratifications are strongly constrained by convection, can serve as a useful simplification for representing the overall effects of convection. We further demonstrate that the dependence of T_s on P_s can be estimated reasonably well with only radiative transfer calculations.

Entrainment and detrainment rates describe the mixing strength between environmental air and cloudy updrafts and are key parameters in many simple models and convective parameterizations. The invariance of the σ coordinate with different surface pressures indicates that the entrainment and detrainment rates should be independent of the air density, thereby supporting the treatment of entrainment and detrainment rate in some convective parameterizations (e.g., Emanuel, 1991; Neggers et al., 2002; Nie & Kuang, 2012; Romps & Kuang, 2010). However, why these rates remain invariant and (more generally) how environmental conditions control them are important issues that require further investigation. Another simplification in this study is the neglect of the radiative effects of clouds. In cases where the changes in clouds are significant, the corresponding radiative effects on determining the atmospheric thermal profiles need to be taken into account. Finally, this study has implications for paleoclimate research. For example, during the early Earth both, the low surface pressure and weak insolation (the faint young Sun) would lead to low surface temperature, contradicting with geological evidences showing similar surface temperature with present climate

(e.g., Kasting, 2010). Thus, our results suggest that other factors, very likely including high concentrations of greenhouse gasses (e.g., CO₂ and CH₄), are required to warm the Earth's climate.

Acknowledgments

The authors thank Martin Singh and an anonymous reviewers for their helpful reviews and Marat Khairoutdinov for making the numerical model available. This research was partially supported by the National Natural Science Foundation of China Grant 41875050 (to J. N.), the Scripps Institutional Postdoctoral Fellowship (to S.H.), and the Earth Institute Fellowship (to D. M.). ERA-Interim reanalysis and GPCP precipitation data can be accessed at <https://apps.ecmwf.int/datasets/> and <https://rda.ucar.edu/datasets/ds728.2/>, respectively. The computations in this paper were run on the Odyssey cluster supported by the FAS Division of Science, Research Computing Group at Harvard University. Primary data and scripts used in the analysis are archived by the Research Computing Group at Harvard University and can be obtained by contacting ithelp@harvard.edu.

References

- Arakawa, A., & Schubert, W. H. (1984). Interaction of a cumulus cloud ensemble with the large-scale environment, Part I. *Journal of the Atmospheric Sciences*, *31*, 674–701.
- Boos, W. R., & Kuang, Z. (2010). Dominant control of the South Asian monsoon by orographic insulation versus plateau heating. *Nature*, *463*, 218–222.
- Bretherton, C. S., & Park, S. (2008). A new bulk shallow-cumulus model and implications for penetrative entrainment feedback on updraft buoyancy. *Journal of the Atmospheric Sciences*, *65*, 2174–2193.
- Dee, D. P. (2011). coauthors The era-interim reanalysis: Configuration and performance of the data assimilation system. *Quarterly Journal of the Royal Meteorological Society*, *137*, 553–597.
- Emanuel, K. A. (1991). A scheme for representing cumulus convection in large-scale models. *Journal of the Atmospheric Sciences*, *48*, 2313–2329.
- Emanuel, K. A., Neelin, J. D., & Bretherton, C. S. (1994). On large-scale circulations in convecting atmospheres. *Quarterly Journal of the Royal Meteorological Society*, *120*, 1111–1143.
- Held, I. M. (1982). On the height of the tropopause and the static stability of the troposphere. *Journal of the Atmospheric Sciences*, *39*, 412–417.
- Holloway, C. E., & Neelin, J. D. (2009). Moisture vertical structure, column water vapor, and tropical deep convection. *Journal of the Atmospheric Sciences*, *66*, 1665–1683.
- Hu, S., & Boos, W. R. (2017a). The physics of orographic elevated heating in radiative-convective equilibrium. *Journal of the Atmospheric Sciences*, *74*, 2949–2965.
- Hu, S., & Boos, W. R. (2017b). Competing effects of surface albedo and orographic elevated heating on regional climate. *Geophysical Research Letters*, *44*, 6966–6973. <https://doi.org/10.1002/2016GL072441>
- Huffman, G. J. (2001). coauthors Global precipitation at one-degree daily resolution from multisatellite observations. *Journal of Hydrometeorology*, *2*, 36–50.
- Kasting, J. F. (2010). *How to find a habitable planet* (326 pp.). PA: Princeton University Press.
- Khairoutdinov, M. F., & Randall, D. A. (2003). Cloud resolving modeling of the ARM summer 1997 IOP: Model formulation, results, uncertainties, and sensitivities. *Journal of the Atmospheric Sciences*, *60*, 607–625.
- Kiehl, J. T., Hack, J. J., Bonan, G. B., Boville, B. A., Williamson, D. L., & Rasch, P. J. (1998). The National Center for Atmospheric Research Community Climate Model: CCM3. *Journal of Climate*, *11*, 1131–1149.
- Kite, E. S., Williams, J. P., Lucas, A., & Aharonson, O. (2014). Low paleopressure of the Martian atmosphere estimated from the size distribution of ancient craters. *Nature Geoscience*, *7*, 335–339.
- Kuang, Z., & Bretherton, C. S. (2006). A mass-flux scheme view of a high-resolution simulation of a transition from shallow to deep cumulus convection. *Journal of the Atmospheric Sciences*, *63*, 1895–1909.
- Ma, D., Boos, W., & Kuang, Z. (2014). Effects of orography and surface heat fluxes on the South Asian summer monsoon. *Journal of Climate*, *27*, 6647–6659.
- Marty, B., Zimmermann, L., Pujol, M., Burgess, R., & Philippot, P. (2014). Nitrogen isotopic composition and density of the Archean atmosphere. *Science*, *342*, 101–104.
- Mlawer, E. J., Taubman, S. J., Brown, P. D., Iacono, M. J., & Clough, S. A. (1997). Radiative transfer for inhomogeneous atmospheres: RRTM, a validated correlated-k model for the longwave. *Journal of Geophysical Research*, *102*, 16,663–16,682.
- Molnar, P., Boos, W. R., & Battisti, D. S. (2010). Orographic controls on climate and paleoclimate of Asia: Thermal and mechanical roles for the Tibetan Plateau. *Annual Review of Earth and Planetary Sciences*, *38*, 77–102.
- Molnar, P., & Emanuel, K. A. (1999). Temperature profiles in radiative-convective equilibrium above surfaces at different heights. *Journal of Geophysical Research*, *104*, 24,265–24,271.
- Neggers, R. A. J., Siebesma, A. P., & Jonker, H. J. J. (2002). A multiparcel model for shallow cumulus convection. *Journal of the Atmospheric Sciences*, *59*, 1655–1668.
- Nie, J., Boos, W. R., & Kuang, Z. M. (2010). Observational evaluation of a convective quasi-equilibrium view of monsoons. *Journal of Climate*, *23*, 4416–4428.
- Nie, J., & Kuang, Z. (2012). Responses of shallow cumulus convection to large-scale temperature and moisture perturbations: A comparison of large-eddy simulations and a convective parameterization based on stochastically entraining parcels. *Journal of the Atmospheric Sciences*, *69*, 1936–1956.
- Nie, J., Kuang, Z. M., Jacob, D. J., & Guo, J. (2016). Representing effects of aqueous phase reactions in shallow cumuli in global models. *Journal of Geophysical Research: Atmospheres*, *121*, 5769–5787. <https://doi.org/10.1002/2015JD024208>
- Pierrehumbert, R. T. (2010). *Principles of planetary climate* (652 pp.). Cambridge, UK: Cambridge University Press.
- Poulsen, C. J., Tabor, C. R., & White, J. D. (2015). Long-term climate forcing by atmospheric oxygen concentrations. *Science*, *348*, 1238–1241.
- Rao, G. V., & Erdogan, S. (1989). The atmospheric heat-source over the Bolivian Plateau for a mean January. *Boundary-Layer Meteorology*, *46*, 13–33.
- Romps, D. M. (2010). A direct measure of entrainment. *Journal of the Atmospheric Sciences*, *67*, 1908–1927.
- Romps, D. M. (2014). An analytical model for tropical relative humidity. *Journal of Climate*, *27*, 7432–7449.
- Romps, D. M., & Kuang, Z. (2010). Nature versus nurture in shallow convection. *Journal of the Atmospheric Sciences*, *67*, 1655–1666.
- Siebesma, A. P., & Cuijpers, J. W. M. (1995). Evaluation of parametric assumptions for shallow cumulus convection. *Journal of the Atmospheric Sciences*, *52*, 650–666.
- Silvers, L. G., Stevens, B., Mauritsen, T., & Giorgetta, M. (2016). Radiative convective equilibrium as a framework for studying the interaction between convection and its large-scale environment. *Journal of Advances in Modeling Earth Systems*, *8*, 1330–1344. <https://doi.org/10.1002/2016MS000629>
- Singh, M. S., Kuang, Z., Maloney, E. D., Hannah, W. M., & Wolding, B. O. (2017). Increasing potential for intense tropical and subtropical thunderstorms under global warming. *Proceedings of the National Academy of Sciences*, *114*, 11,657–11,662.
- Singh, M. S., & O’Gorman, P. A. (2012). Upward shift of the atmospheric general circulation under global warming: Theory and simulations. *Journal of Climate*, *25*, 8259–8276.

- Singh, M. S., & O'Gorman, P. A. (2013). Influence of entrainment on the thermal stratification in simulations of radiative-convective equilibrium. *Geophysical Research Letters*, *40*, 4398–4403. <https://doi.org/10.1002/grl.50796>
- Som, S. M., Buick, R., Hagadorn, J. W., Blake, T. S., Perreault, J. M., Harnmeijer, J. P., & Catling, D. C. (2016). Air pressure 2.7 billion years ago limited to less than half modern levels by gas bubbles in basalt. *Nature Geoscience*, *9*, 448–452.
- Wu, G. X. (2007). Coauthors The influence of mechanical and thermal forcing by the Tibetan Plateau on Asian climate. *Journal of Hydrometeorology*, *8*, 770–789.
- Wu, G. X., & Zhang, Y. (1998). Tibetan Plateau forcing and the timing of the monsoon onset over South Asia and the South China Sea. *Monthly Weather Review*, *126*, 913–927.

Similarity among atmospheric thermal stratifications over elevated surfaces under Radiative-Convective Equilibrium

Ji Nie¹, Yan Xia¹, Shineng Hu², Jun Yang¹, and Ding Ma³

1: Department of Atmospheric and Oceanic Sciences, Peking University, Beijing, China

2: Scripps Institution of Oceanography, University of California San Diego, La Jolla, California

3: Earth Institute, Columbia University, New York, New York

Supporting Information

Contents of this file

Figures S1 to S3

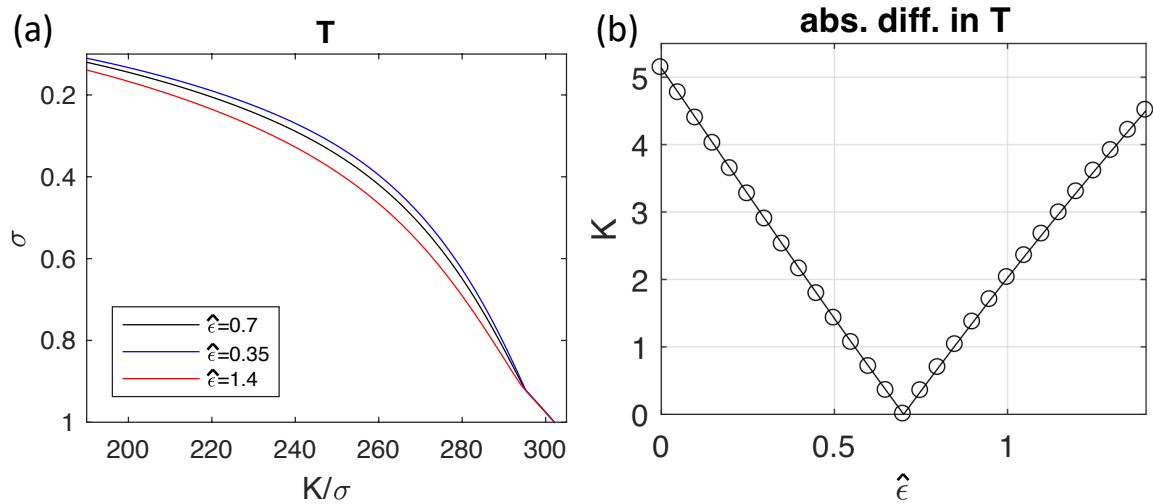


Figure S1. (a) Temperature profiles calculated using the plume model with $\hat{\epsilon} = 0.35$, $\hat{\epsilon} = 0.7$, and $\hat{\epsilon} = 1.4$, respectively. (b) The absolute values of temperature changes as $\hat{\epsilon}$ varies from 0 to 1.5. The temperature changes are calculated as the temperature anomalies to the $\hat{\epsilon} = 0.7$ case averaged between $\sigma = 1$ and $\sigma = 0.2$ level). All the calculations are for the $P_s = 500$ hPa case.

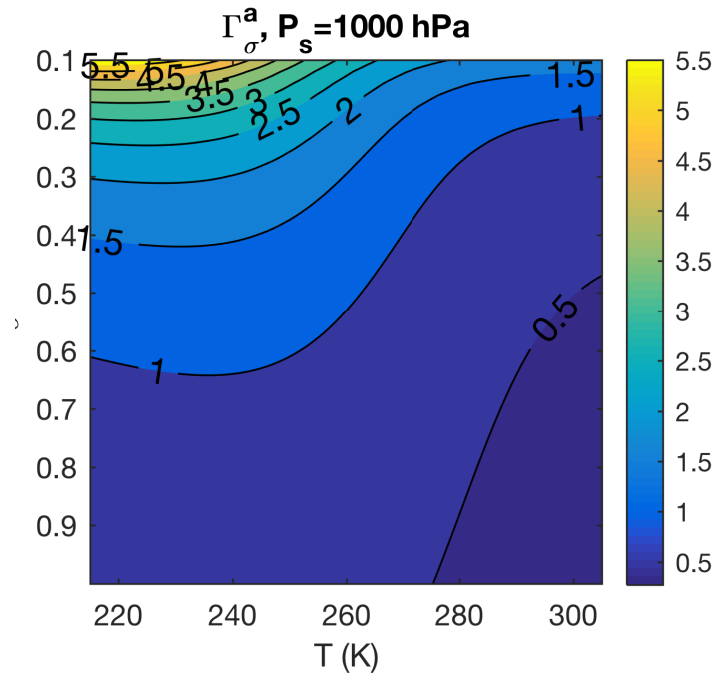


Figure S2. Moist adiabatic lapse rates in σ (Γ_{σ}^a , units of $\text{K}/0.01\sigma$) as functions of the temperature (x-axis) and pressure (y-axis is σ). The calculation is for the $P_s = 1000 \text{ hPa}$ case.

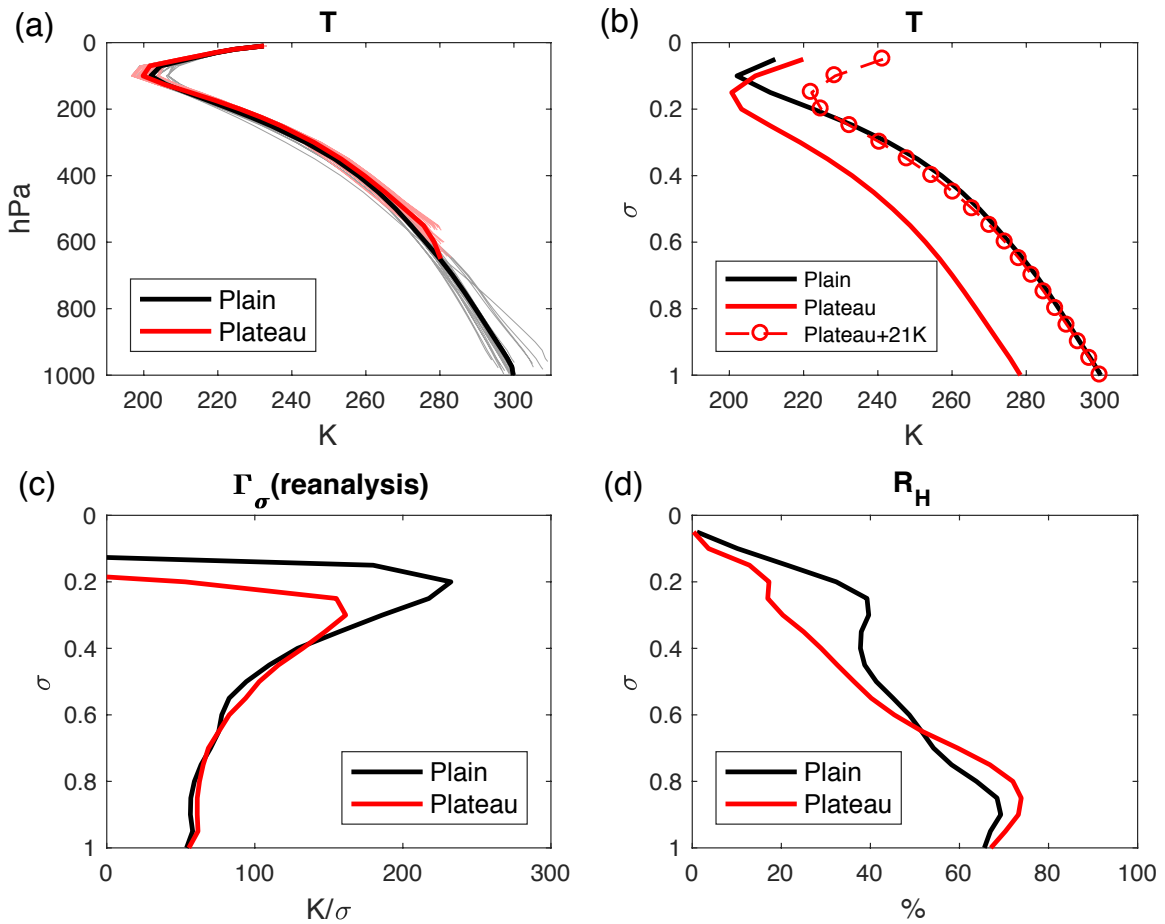


Figure. S3. Similar to Fig. 5, except the plain regions include only areas in Asia (an area of approximately $1.4 \times 10^6 \text{ km}^2$). Note that the number of thin grey lines is smaller than that in Fig. 5a due to the reduction in the sampling size.